SCIENCE ROBOTICS | RESEARCH ARTICLE

BIOMIMETICS

Laser-assisted failure recovery for dielectric elastomer actuators in aerial robots

Suhan Kim[1,2]†, Yi-Hsuan Hsiao[1,2]†, Younghoon Lee[1,2], Weikun Zhu[2,3], Zhijian Ren[1,2], Farnaz Niroui[1,2], Yufeng Chen[1,2]*

Insects maintain remarkable agility after incurring severe injuries or wounds. Although robots driven by rigid actuators have demonstrated agile locomotion and manipulation, most of them lack animal-like robustness against unexpected damage. Dielectric elastomer actuators (DEAs) are a class of muscle-like soft transducers that have enabled nimble aerial, terrestrial, and aquatic robotic locomotion comparable to that of rigid actuators. However, unlike muscles, DEAs suffer local dielectric breakdowns that often cause global device failure. These local defects severely limit DEA performance, lifetime, and size scalability. We developed DEAs that can endure more than 100 punctures while maintaining high bandwidth (>400 hertz) and power density (>700 watt per kilogram)—sufficient for supporting energetically expensive locomotion such as flight. We fabricated electroluminescent DEAs for visualizing electrode connectivity under actuator damage. When the DEA suffered severe dielectric breakdowns that caused device failure, we demonstrated a laser-assisted repair method for isolating the critical defects and recovering performance. These results culminate in an aerial robot that can endure critical actuator and wing damage while maintaining similar accuracy in hovering flight. Our work highlights that soft robotic systems can embody animal-like agility and resilience—a critical biomimetic capability for future robots to interact with challenging environments.

INTRODUCTION

Flight is one of the most energetically demanding locomotion modes. Birds and aerial insects navigate, feed, and evade predators in complex and dangerous environments where they often encounter unexpected injuries. To survive in nature, these animals exhibit remarkable resilience to flight muscle (*1*) and wing (*2*) damage caused by predator attacks (*3*) and general wear (*4*). Motivated by applications such as exploration of cluttered and constrained environments, researchers have developed micro aerial vehicles (MAVs) that can endure in-flight collisions using impact-resilient mechanisms such as collapsible wings (*5*) and origami cages (*6*). In addition, flight controllers have been designed to compensate for unexpected damage of MAV propellers (*7*) or wings (*8*). However, unlike natural flight muscles, rigid flight actuators (*9*, *10*) cannot tolerate punctures or incision damage, which limits MAVs′ robustness when they perform high-risk missions.

In contrast to rigid motors, muscle-like soft actuators (*11*, *12*) are essential for constructing animal-like damage-resilient robots (*13*, *14*). A wide range of self-healing materials (*15*) have been developed for restoring mechanical strength (*16*) and electrical connectivity (*13*). In pneumatic grippers, self-healing elastomers (*17*) can remove perforations and leaks after undergoing heat treatment. For soft robots powered by hydraulically amplified self-healing actuators (*18*), dielectric fluids can tolerate electrical breakdown. However, to achieve self-healing properties, most materials and designs make compromises in having higher damping coefficients (viscoelasticity or viscosity), which result in limited power density (<200 W kg^{-1}). Although existing self-healing actuators have demonstrated damage resilience in numerous soft robotic systems, they cannot achieve flight because of limited bandwidth (<100 Hz) and controllability. Embodying animal-like agility and resilience in an aerial robot remains a major unaddressed challenge.

Achieving damage-resilient flight requires power-dense and fault-tolerant actuators. Dielectric elastomer actuators (DEAs) (*19*, *20*) are the most power-dense (>500 W kg^{-1}) soft actuators, and they have enabled agile robotic locomotion in aquatic (*21*), terrestrial (*22*), and aerial (*20*) environments. However, because of the presence of localized defects, most DEAs suffer dielectric breakdown and short life span when they operate at peak performance conditions or experience unexpected damage. Severe local defects can cause global device failure, which is the major limiting factor of DEA lifetime and size scalability. To endure the dielectric breakdowns caused by defects or damage, self-clearing electrodes (*23*–*25*) have been developed for DEAs. Self-clearing is a mechanism where the electrode surrounding a defective site degrades under an applied current, and this effect isolates the local damage from the bulk electrode. Although existing studies (*23*, *26*) have demonstrated DEA resilience against minor defects and damage, self-clearing cannot isolate severe defects that have low resistance and dielectric strength. After a DEA is pierced by a needle (*23*), the maximum strain is reduced by more than 60% compared with that of an undamaged DEA. This substantial actuation performance reduction would prevent a robot from performing energetically expensive tasks such as flight. Besides self-clearing, other self-healing materials and designs (*27*, *28*) have been incorporated to improve actuator resilience. However, these alternative approaches make a trade-off between DEA performance and resilience. Their energy and power density remain substantially lower (<50%) than the best-performing DEAs (*19*, *20*). The major challenge of enabling damage-

---

[1] Department of Electrical Engineering and Computer Science, Massachusetts Institute of Technology, 77 Massachusetts Avenue, Cambridge, MA 02139, USA. [2] Research Laboratory of Electronics, Massachusetts Institute of Technology, 77 Massachusetts Avenue, Cambridge, MA 02139, USA. [3] Department of Chemical Engineering, Massachusetts Institute of Technology, 77 Massachusetts Avenue, Cambridge, MA 02139, USA.
*Corresponding author. Email: yufengc@mit.edu

†These authors contributed equally to this work.

resilient flight is to develop fault-tolerant actuators without compromising key performance metrics such as power density and controllability.

In this work, we proposed the design, fabrication, and repair methods that led to soft artificial flight muscles capable of enduring severe damage. First, we optimized the DEA electrode by investigating the effects of carbon nanotube (CNT) concentration on self-clearing properties and device power density. The DEA can endure more than 100 punctures while it maintains high power density (>700 W kg^{-1}) for sustaining controlled flight. Second, we developed a laser repair method that can isolate unclearable breakdowns in failed DEAs. We demonstrated an experimental technique where electrode connectivity can be visualized through electroluminescence. By combining laser ablation and self-clearing, this repair method can reliably isolate defects and recover DEA performance, which substantially improves DEA lifetime and resilience.

To illustrate the effectiveness of our methods, we constructed an insect-scale flapping-wing robot using damaged DEAs. After enduring severe piercing damage, unclearable breakdowns, and a 20% loss of wing area, the robot demonstrated a 12-s feedback-controlled flight (Movie 1) with a maximum position error of 3.56 cm (0.7 body length). Here, an aerial robot endured critical actuator damage and demonstrated hovering flights of similar position and attitude accuracy. This result not only represents a challenging biomimetic capability that is absent in existing robots but also highlights the unique advantages of applying soft artificial muscles in place of traditional rigid actuators.

RESULTS

Design of a damage-resilient aerial robot

We designed a damage-resilient robot for flying in hazardous environments (Fig. 1A). The robot (Fig. 1B) consisted of four flapping-wing modules that were independently driven by rolled multilayer DEAs. To induce damage similar to that experienced by biological flyers, we pierced the flight actuator (*29*) and removed wing tip areas (*30*). Specifically, the robot could endure three types of severe damage that would be catastrophic for existing aerial robots (*9*, *10*). First, the actuator maintained flight-level performance after it was pierced by 10 needles (Fig. 1C), which was equivalent to suffering more than 100 punctures in the elastomer-electrode multilayer (figs. S1 to S3). Second, laser ablation isolated unclearable breakdowns and recovered 87% of blocked force of a previously failed DEA (Fig. 1D). Third, the actuator tolerated asymmetric aerodynamic loading when one of the two robot wings lost 20% of its wing area (Fig. 1E). These damage-resilience properties were enabled by our proposed DEA design, fabrication, and repair methods. Under piercing damage (Fig. 1C) and unclearable breakdowns (Fig. 1D), the DEAs maintained sufficient free displacement and blocked force (Fig. 1, F and G, and fig. S2) for sustaining flight. Despite enduring severe damage, these DEAs maintained a lifetime of more than 1 million actuation cycles when driven at the flight conditions of 1500 V and 400 Hz (fig. S1D).

Optimal electrode design for enduring piercing damage

We optimized the DEA electrode so that the DEA could maintain flight capabilities after it endured severe piercing damage. Our DEA (*20*) consisted of alternating CNT electrodes and transparent elastomer layers (Fig. 2A). When a needle pierced a DEA, it displaced local CNTs, introduced particulates, and trapped air pockets. These defects induced two problems: local electrical shorting and reduction of dielectric strength. Our DEA removed electrical shorting through self-clearing (*23*–*26*)—a process that drove current through the defect and thermally degraded local electrical connectivity (Fig. 2A). To mitigate dielectric strength reduction at the defect site, we optimized the quantity of CNTs applied on the DEA electrodes.

We designed experiments to quantify self-clearing efficacy against piercing damage. Specifically, we prepared a resistive

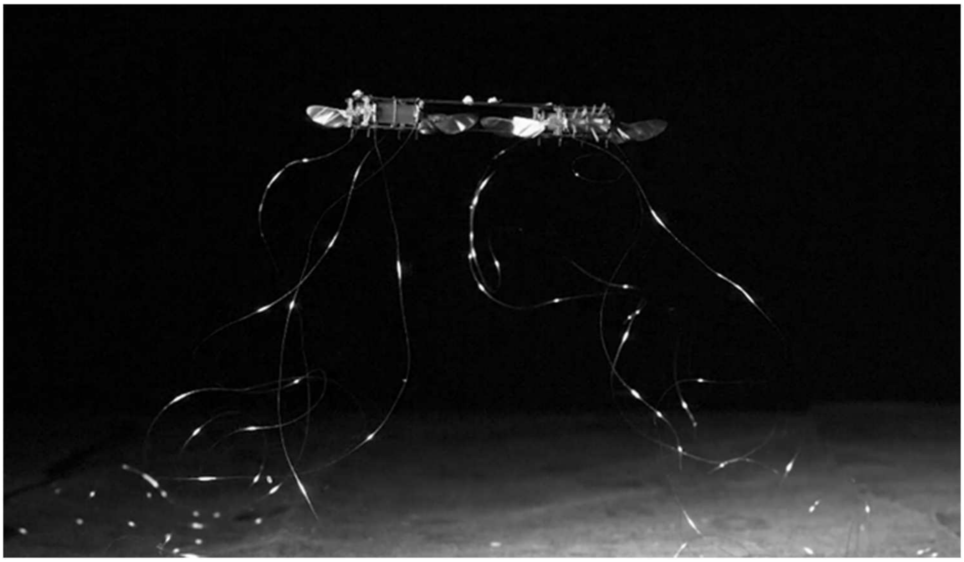

Movie 1. Hovering flight of a robot driven by 10-pierced and laser-recovered DEAs with a damaged wing. A 12-s hovering flight performed by a robot with damaged DEAs and wing. This robot was driven by two undamaged DEAs, a 10-pierced DEA, and a laser-recovered DEA. One robot wing also suffered 20% loss of the wing area.

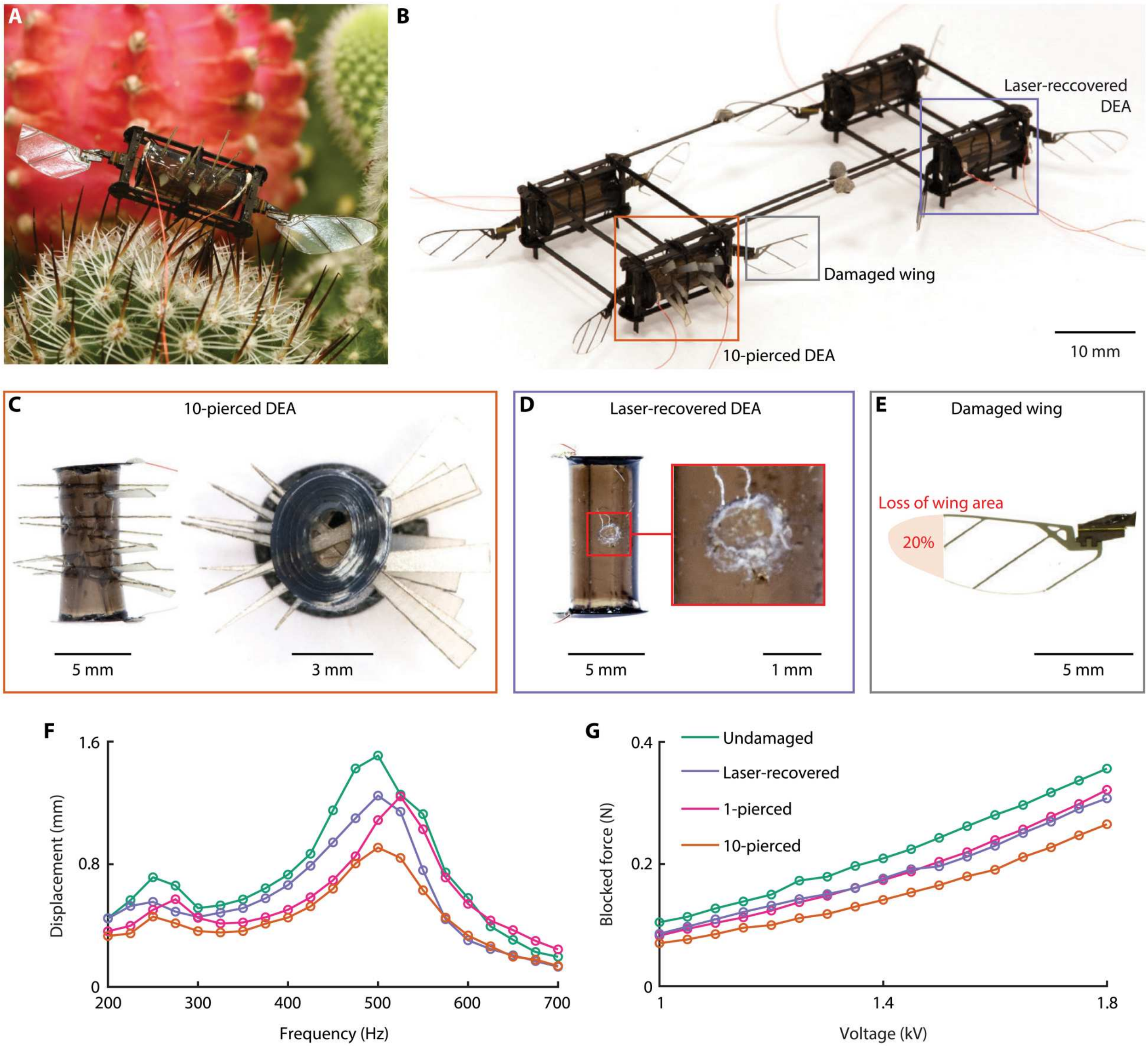

Fig. 1. A DEA-driven damage-resilient aerial robot. (**A**) A photograph illustrating a damaged biomimetic robot module that landed on a cactus. (**B**) The aerial robot consisted of four modules that could endure severe damage (C to E) while maintaining controlled flight capability. (**C**) A rolled DEA was pierced by 10 fiberglass needles. (**D**) A DEA that suffered severe burning damage. To recover its performance, the DEA was unrolled, laser ablated, electrically reconnected, self-cleared, rerolled, and reinstalled into the robot. (**E**) A damaged robot wing lost 20% of its area near the wing tip. (**F** and **G**) Comparisons of DEA's free displacement (F) and blocked force (G) among undamaged, laser-recovered, and pierced DEAs.

sample that consisted of a single CNT layer embedded in elastomer (Fig. 2B). We pierced the sample with a conductive needle, which created a shorted path between the needle and the resistive sample. Then, we applied a voltage across this path and leveraged self-clearing to isolate the defects (Fig. 2B). In this experiment (Fig. 2C), we measured electrode (R_{CNT}) and contact (R_{contact}) resistances before and after self-clearing (fig. S1E). We observed that the induced current thermally degraded CNTs in the vicinity of the needle and caused R_{contact} to become an open circuit. In addition, we confirmed that the electrode resistance (R_{CNT}) remained unchanged (Fig. 2D), suggesting that self-clearing had negligible influence on the CNT bulk resistance.

In addition to removing electrical shorting (Fig. 2, B to D), we quantified the influence of CNT areal density on reducing the dielectric strength at the defect site. In the experiment (Fig. 2C), we continued to increase the applied voltage until a permanent breakdown was observed (fig. S1F). We found that as the CNT areal density increased, the sample sheet resistance and defect breakdown voltage decreased (Fig. 2E). This measurement highlighted a design trade-off: A reduction of CNT areal density improved the defect's dielectric strength but increased sheet resistance, which reduced DEA efficiency and bandwidth. On the basis of this measurement, we calculated the optimal CNT areal density (highlighted region in Fig. 2E) that maximized a DEA's damage resilience while satisfying actuation bandwidth and force as required by flight (see

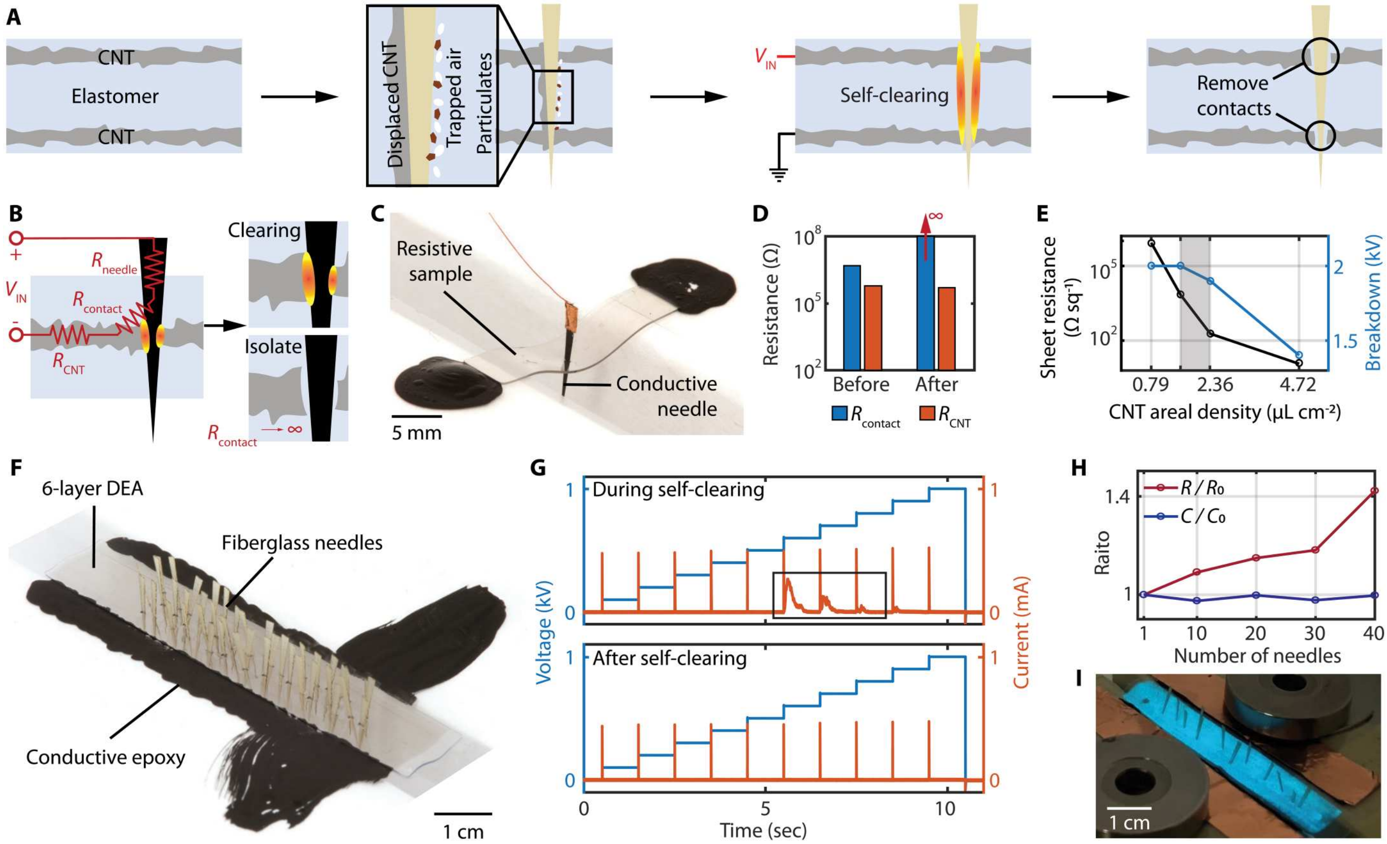

Fig. 2. Self-clearing of piercing damage in CNT electrodes. (**A**) Illustration of defect isolation through self-clearing. (**B** and **C**) Illustration (B) and experiment (C) of defect isolation in a resistive sample. (**D**) Contact ($R_{contact}$) and bulk CNT (R_{CNT}) resistances before and after self-clearing. (**E**) Electrode sheet resistance and dielectric strength as functions of CNT areal density. (**F**) An unrolled DEA was pierced by 40 fiberglass needles. (**G**) Applied voltage and measured current during and after self-clearing. The boxed region corresponds to thermal degradation of defects. (**H**) Change in DEA's resistance and capacitance as functions of puncture counts. (**I**) Piercing test of an electroluminescent DEA showed that the bulk electrode connectivity was unaffected.

Supplementary Discussion S1 and fig. S3 for details on CNT areal density optimization).

To validate this design, we fabricated a six-layer DEA and pierced it with 40 needles (Fig. 2F). We applied self-clearing each time a needle pierced through the DEA (Fig. 2G). The corresponding current response illustrated the removal of local defects (boxed region in Fig. 2G). In addition, we measured DEA resistance and capacitance as a function of repeated piercing damage (Fig. 2H). The DEA resistance refers to the net resistance measured from the device terminals, and it is mainly contributed by R_{CNT} and R_{contact}. When pierced by a small number (<5) of needles, the DEA experienced negligible resistance increase, because the CNT resistivity remained unchanged. As the number of needles increased, local damage caused by nearby needles connected to form a larger defect. Current conduction needed to bypass these damaged sites, which increased the effective conduction length. Hence, the device resistance increased by more than 40% after it was pierced by 40 needles (Fig. 2H). Although there was a moderate increase in DEA resistance, the DEA capacitance remained nearly unchanged. This result implied that the self-clearing process did not degrade the electrode's bulk connectivity and coverage, which are related strongly to the DEA output force and displacement. To confirm this finding, we fabricated an electroluminescent DEA whose active area emitted light during high-frequency (400-Hz) actuation. When the DEA was pierced, no loss of illumination was observed surrounding the damaged sites, indicating no detrimental damage to the electrode and its function (Fig. 2I and movie S1). We further quantified a rolled DEA's damage resilience. The DEA's free displacement and blocked force were reduced to 60 and 74%, respectively, of the undamaged levels (Fig. 1, F and G) after it was pierced by 10 needles (Fig. 1C). Compared with the blocked force, the free displacement experienced a larger reduction due to the mechanical influence of the needles in the DEA (fig. S2, E to G).

Laser-assisted isolation of unclearable defects

In addition to optimizing the self-clearing mechanism, we developed a laser ablation method for isolating unclearable defects. Unclearable defects refer to permanent dielectric breakdown that cannot be isolated through the self-clearing process alone (Fig. 3A). In the previous section, clearable defects were created by thin needles that pierced through very small areas (<0.05 mm^2) of electrode and elastomer. The self-clearing process disconnected local damaged electrode to recover DEA performance. In contrast, unclearable defects were caused by major damage to the elastomer, such as removing dielectric elastomer materials or

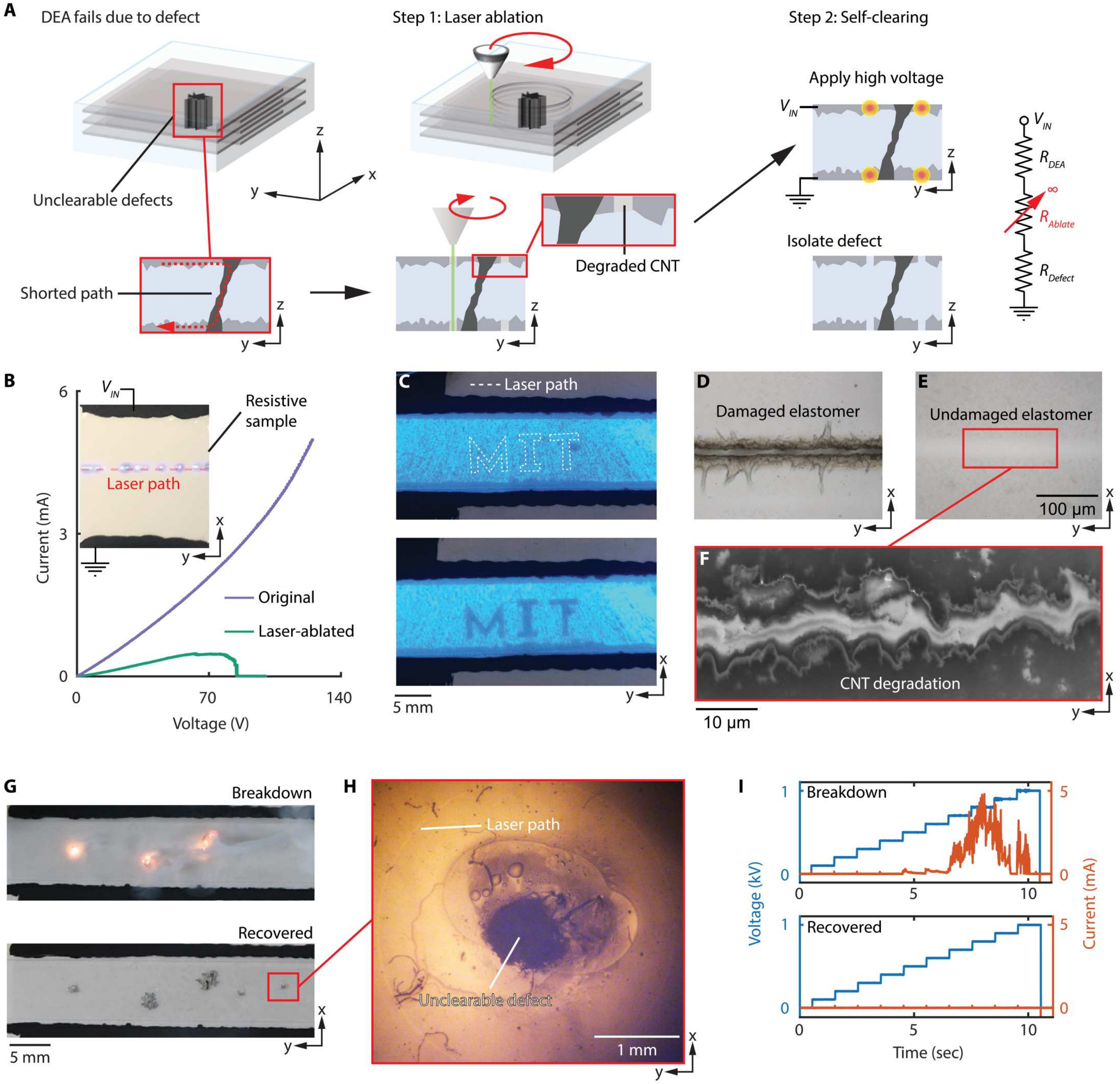

Fig. 3. Combination of laser ablation and self-clearing for isolating unclearable damage. (**A**) Illustration of the two-step defect isolation method. (**B**) Self-clearing occurred along the laser-ablated path and electrically disconnected a resistive sample. (**C**) This method disconnected selective regions in an electroluminescent DEA. (**D**) The elastomer was damaged at high (>1.2-W) laser power. (**E** and **F**) At intermediate laser power (0.7 to 1.2 W), the elastomer was undamaged (E), whereas the CNTs were degraded (F). (**G**) Comparison of a DEA before and after defect isolation under a 1-kV input. (B) to (H) represent the top view images of the DEA. (**H**) A laser-ablated contour enclosed the unclearable defect. (**I**) Applied voltage and current response before and after defect isolation.

burning the elastomer-electrode multilayer for an extended duration (>0.5 s). The resultant defect either became an electrical bridge or suffered reduced dielectric strength. Applying a voltage across the defect would cause continued burning and further degrade the surrounding electrodes and elastomer. Although an unclearable defect occupied a small area (0.1 to 10 mm^2) within the 400-mm^2 elastomer-electrode multilayer, this local damage could cause permanent DEA failure.

We developed a two-step process for recovering a DEA that had an unclearable defect (fig. S4). First, we used a diode-pulsed solid-state (DPSS) laser to trace an enclosed contour around the defect (Fig. 3A). The laser beam penetrated the elastomer-electrode multilayer, and most of the energy was absorbed by CNTs along the laser path, causing thermal degradation of the CNTs surrounding the defect. Second, we applied a high voltage across the DEA to remove the degraded CNTs through self-clearing (Fig. 3A). This process electrically disconnected the unclearable defect from the rest of the DEA, leading to DEA performance recovery (see Supplementary Discussion S2 and fig. S5 and S6 for a detailed electrical model). Although the defect might only exist in one elastomer layer, this process disconnected all six layers of the CNTs enclosed within the laser-ablated contour. Despite having this limitation, the disconnected area occupied 0.1 to 5% of the net electrode area, which did not lead to substantial performance reduction.

To validate this method and optimize the laser ablation parameters, we designed experiments using resistive (Fig. 3B) and capacitive (Fig. 3C) test samples. Figure 3B compares the current-voltage relation (I-V) characteristics of resistive samples with or without laser ablation. As shown in the top view illustration (Fig. 3B), we varied the input voltage V_{IN} and measured the current response. The original sample's I-V characteristic was approximately linear. After the test sample was laser-ablated across a horizontal path, we observed a substantial increase in net resistance. In addition, as the input voltage increased, the test sample experienced self-clearing along the laser path and eventually became electrically disconnected (Fig. 3B). We observed small but visible sparks (inset of Fig. 3B and movie S2) during the self-clearing process. This result showed that self-clearing occurred along the laser-ablated path and did not affect other electrode areas. We further fabricated electroluminescent capacitive samples to visualize electrode connectivity under laser ablation and self-clearing. The laser beam traced the outer contour of three letters, "MIT," and then the capacitive sample was driven by a high-frequency voltage signal. During this self-clearing process, the regions enclosed by the laser contour became disconnected, and the corresponding letters MIT became dark (Fig. 3C and movie S3). The laser ablation process required specific pulse energy, repetition rate, and beam spot size. Although a low-power (<0.7 W) cut could not sufficiently degrade the CNTs (fig. S4F), an excessively high-power (>1.2 W) cut could severely damage the elastomer (Fig. 3D and fig. S4D). For an unrolled 200-μm-thick DEA sheet that consisted of six CNT layers, we found the optimal laser power, pulse frequency, and spot size to be 1.0 W, 80 kHz, and 30 μm, respectively. The laser beam was focused on the top surface of the elastomer-electrode multilayer. Under these conditions, the top view confocal microscope image showed that the elastomer was undamaged (Fig. 3E), and the top view scanning electron microscope image highlighted CNT degradation along the laser path (Fig. 3F).

This laser-assisted method enabled DEA recovery (Fig. 3, G to I). In an unrolled DEA sample, we introduced five unclearable defects where self-clearing alone induced intense burning (Fig. 3G and movie S4). Then, we isolated all five defects through laser ablation (Fig. 3H) and self-clearing. The DEA was recovered, and it no longer experienced shorting or breakdown (Fig. 3I). These experiments showed that the combination of laser ablation and self-clearing could isolate unclearable defects in a DEA. Furthermore, we fabricated a rolled DEA that had an unclearable defect (Fig. 1D). After conducting laser ablation and self-clearing (movie S5), the DEA's

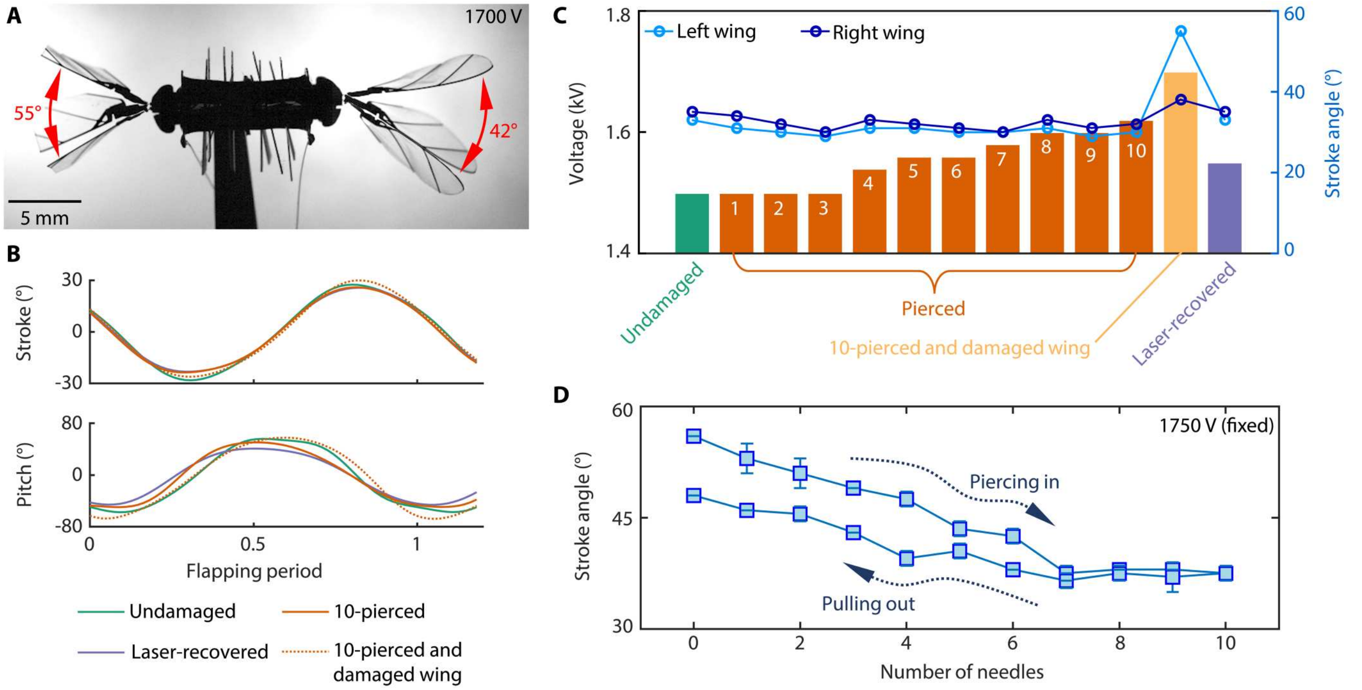

Fig. 4. Characterization of DEA damage resilience in static flapping-wing experiments. (**A**) A composite image of the robot flapping-wing kinematics. The DEA was pierced by 10 needles, and the left wing lost 20% of its area. (**B**) Robots with differently damaged actuators and wings could produce wing stroke and pitch motions that correspond to liftoff conditions. (**C**) Robot wing stroke amplitude at different damage conditions and driving voltages. Under DEA piercing damage, unclearable breakdowns, and wing damage labeled along the *x* axis, the robot maintained similar wing stroke motions when the driving voltage was increased. These flapping kinematics conditions correspond to the liftoff conditions. (**D**) Degradation and recovery of robot stroke amplitude when needles were sequentially put in and then removed from the DEA. The error bars indicate the measured left- and right-wing stroke angles.

free displacement and blocked force recovered to 83 and 87% that of an undamaged DEA (Fig. 1, F and G).

Robot flight demonstrations after experiencing severe damage

The puncture-tolerant DEAs and laser-assisted repair method enabled damage resilience in our aerial robots. We conducted static flapping (Fig. 4, fig. S7, and movie S6), liftoff (Fig. 5, fig. S8, as well as movies S7 and S8), and hovering flight (Figs. 6 and 7, fig. S9 and S10, Movie 1, as well as movies S9 and S10) experiments using a biomimetic insect-scale flapping-wing robot. In static flapping experiments, we compared the wing kinematics of three robots each driven by an undamaged DEA, a laser-recovered DEA (Fig. 1D), or a 10-pierced DEA (Fig. 1C). In these experiments, we operated the robot at 400 Hz and extracted the wing stroke and pitch motions from the recorded high-speed videos. For the 10-pierced DEA, we measured the robot performance each time a subsequent needle pierced through the actuator. After the DEA was pierced 10 times, we removed 20% of the robot's left wing and measured performance degradation. Figure 4A shows a composite image of the robot's flapping-wing kinematics at the operating condition of 1700 V and 400 Hz. The instantaneous wing stroke and pitch motions of the robot's right wing are shown in Fig. 4B (dotted orange lines), which correspond to the liftoff condition. Because of the 20% loss of left-wing area, the left- and right-wing motions became asymmetric (Fig. 4, A and C). Unlike rigid actuators (*10*, *31*) that were sensitive to changing loads near resonance conditions, the DEA could easily tolerate unbalanced aerodynamic and inertial loads applied on its two ends. The DEA continued to operate even if the entire left wing was removed (fig. S7E), but extreme wing asymmetry substantially reduced net lift force and deteriorated the robot's flight capability. We also conducted flapping experiments for robots driven by the undamaged or the laser-recovered DEAs. We varied the driving voltage until the robots could exhibit wing stroke and pitch motions (Fig. 4B) that correspond to liftoff. Figure 4C illustrates the wing stroke amplitudes and driving voltages under each damage condition. Compared with an undamaged DEA, the laser-recovered and the 10-pierced DEA required 5 and 10% higher voltages to generate similar wing kinematics (Fig. 4C). These experiments suggested that the DEAs could endure severe damage and preserve sufficient power density for achieving flight.

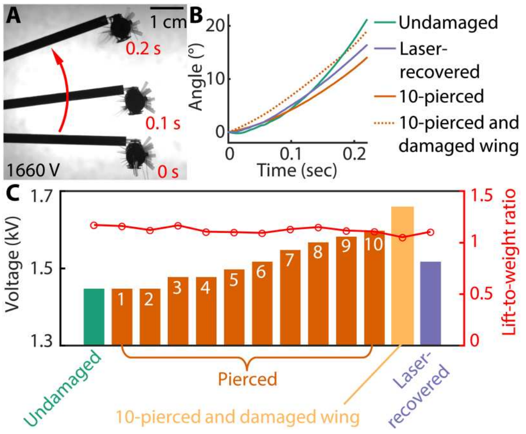

Fig. 5. Robot liftoff experiments under DEA and wing damage. (**A**) A liftoff demonstration performed by the same robot as in Fig. 4A. (**B**) Tracked beam angles during robot liftoff demonstrations. These liftoff experiments correspond to the static flapping-wing conditions in Fig. 4B. (**C**) Measured robot lift-to-weight-ratios at different damage conditions and driving voltages. Under different DEA and wing damage conditions, the robot net lift force remained higher than the robot weight.

To quantify DEA degradation as a function of piercing damage, we conducted another set of flapping-wing experiments in which we measured robot stroke motion reduction under a fixed driving condition (Fig. 4D). Specifically, we drove the robot at 1750 V and 400 Hz while sequentially inserting needles into the DEA. In this process, the robot wing stroke amplitude was reduced from 56° to 38° (Fig. 4D), which corresponded to a 32% reduction in DEA displacement. After the DEA was pierced by 10 needles, we sequentially removed the needles, commanded self-clearing, and then measured wing stroke motion again (Fig. 4D). We observed DEA performance recovery in this process. After all 10 needles were removed, the stroke amplitude recovered to 48°, which represented 86% of the undamaged performance. These experiments suggested that the needle's inertial and constraining effects also deteriorated DEA performance. The details of the experimental setup and flapping-wing test results are described in Supplementary Discussion S3, fig. S7, and movie S6.

We further conducted liftoff experiments to quantify robot lift force reduction as a function of DEA and wing damage (Fig. 5, fig. S8, as well as movies S7 and S8). We mounted the robot on a custom liftoff stand (fig. S8B) where it was constrained to move along the vertical direction. The inertia of the liftoff stand was balanced around a pivot, and the robot could ascend upward if its lift force exceeded its weight. Without any damage, a robot could achieve liftoff at a driving voltage of 1450 V (green bar graph in Fig. 5C). Next, we pierced the DEA, applied self-clearing, and measured the new liftoff voltage. We sequentially pierced the DEA with 10 needles and observed that the liftoff voltage increased to 1600 V (fig. S8C and movie S8). After this test, we replaced one robot wing with a damaged wing and observed another 60-V increase in the liftoff voltage (Fig. 5A). On the basis of the liftoff video, we measured the beam rotation angle (Fig. 5B) and calculated the robot's net lift (Fig. 5C). We repeated the liftoff test for robots driven by the undamaged DEAs and the laser-recovered DEA (Fig. 5, B and C). For the DEA that had an unclearable breakdown (Fig. 1D), the laser-ablated contour disconnected 4.9% of its net electrode area. In the liftoff test, we observed a 5% increase in liftoff voltage, which showed similar lift force to that of a five-pierced DEA (Fig. 5C). These experiments confirmed that the robot preserved the liftoff capabilities after enduring severe damage.

On the basis of these results, we performed three types of hovering flights to evaluate actuator controllability under robot damage. Our 680-mg robot required external power supply, motion tracking, and computation (*20*). The robot consisted of four modules (Fig. 1B) and four pairs of wings and wing hinges. All flights consisted of a 1-s takeoff, a 10-s hover, and a 1-s descent. The robot's flight time was mainly limited by its hinge lifetime, which required replacement every 100 s. First, an undamaged robot demonstrated a 12-s hovering flight (Fig. 6, A to D, and movie S9) 10 cm above the ground. The maximum altitude, position, and attitude errors were 1.23 and 3.51 cm and 3.39°, respectively. Next, we pierced the DEA with a needle (Fig. 6, E to G). To isolate this local piercing damage, we commanded self-clearing (Fig. 6H and

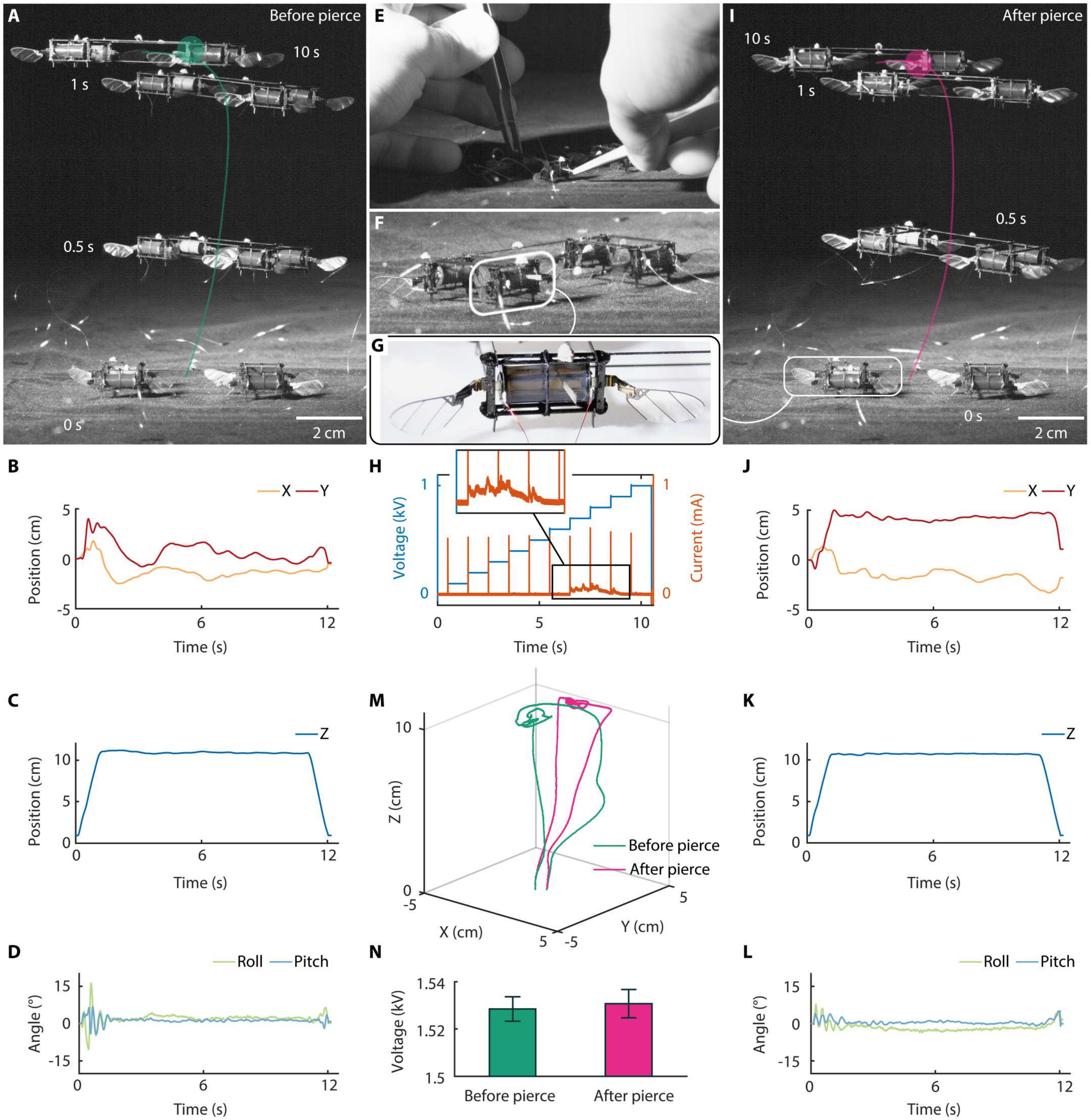

Fig. 6. Flight comparison of robots driven by undamaged and one-pierced DEAs. (**A**) A composite image that shows a 12-s flight performed by an undamaged robot. (**B** to **D**) Robot *x*, *y*, and *z* positions and attitudes that correspond to the flight in (A). (**E**) A fiberglass needle pierced through a DEA. (**F** to **H**) The damaged DEA used self-clearing to isolate the defect. (**I**) A composite image that shows a 12-s flight performed by the damaged robot. (**J** to **L**) Robot *x*, *y*, and *z* positions and attitudes that correspond to the flight in (I). (**M**) Comparison of flight trajectories between the damaged and the undamaged robot. (**N**) Comparison of average DEA operating voltages during the two hovering flights.

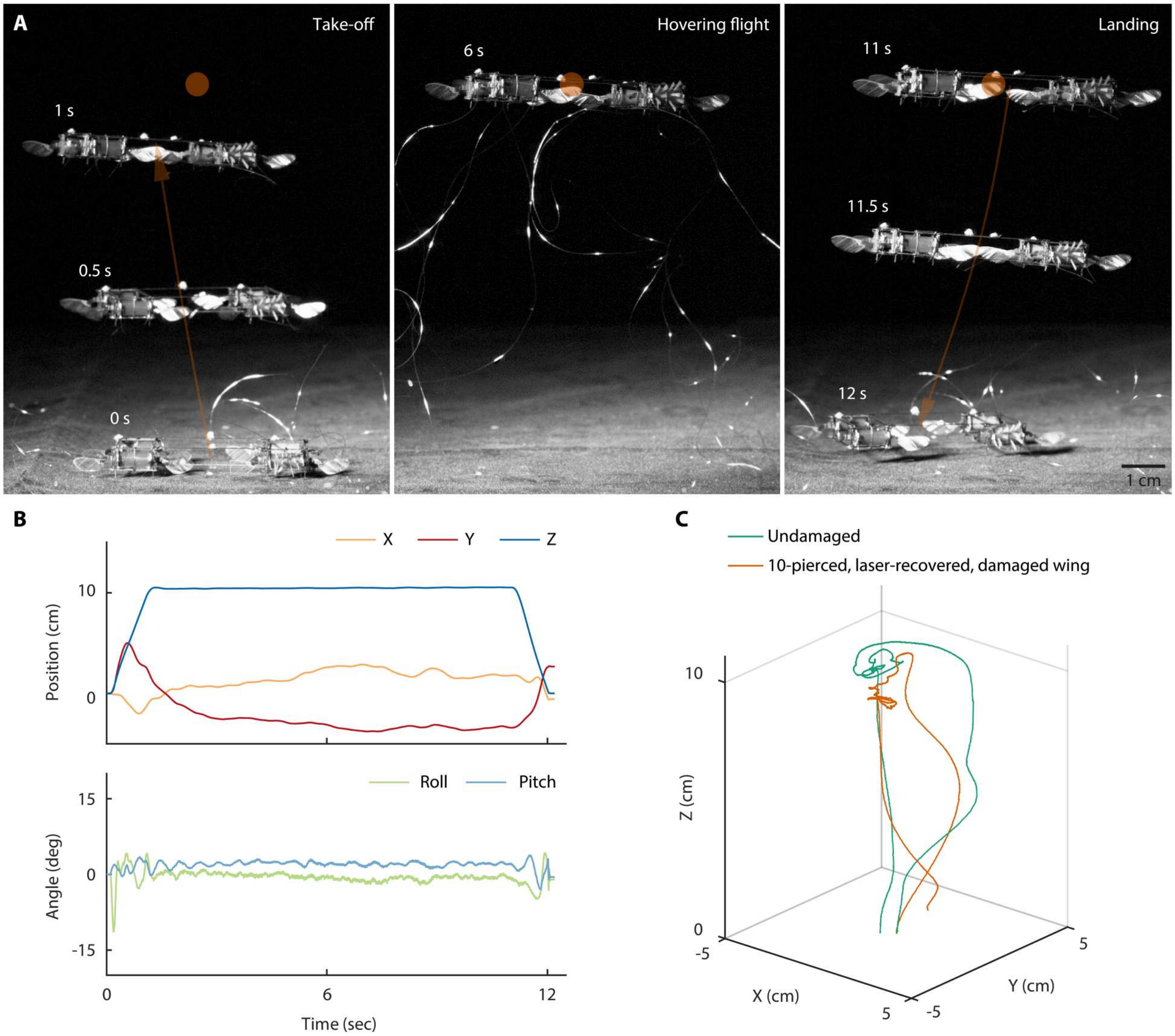

Fig. 7. Flight performance of a severely damaged soft-actuated aerial robot. (**A**) A 12-s hovering flight performed by the severely damaged robot shown in Fig. 1B. One DEA was pierced by 10 needles, the other DEA suffered an unclearable breakdown, and one robot wing lost 20% of its area. In this flight, the robot showed a 1-s ascent (left), a 10-s hover (center), and a 1-s descent (right). (**B**) Tracked robot positions and attitudes corresponding to the flight in (A). (**C**) Flight trajectory comparison of the two robots with or without damage.

movie S9), and the DEA current response showed DEA recovery (Fig. 6H). Then, we performed a short (3-s) test flight to verify robot flight capability (movie S9). Last, we demonstrated a 12-s hovering flight (Fig. 6, I to L) with the damaged robot and achieved similar position and attitude accuracy. Under damage from one piercing, the robot's maximum altitude, position, and attitude error became 1.43 and 4.78 cm and 4.34°, respectively. Figure 6M compared the two flight trajectories before and after the piercing damage. Under damage, the robot maximum position error increased by 34%. This error was reduced after tuning of the controller parameters (fig. S9 and table S1). Figure 6N compared the DEA operating voltage during these hovering flights. On average, the piercing damage led to a 5-V increase in operating voltage during flight. All of these flight experiments were conducted without requiring robot repair or flight controller tuning. This result showed that the robot can easily tolerate minor actuator damage. Figure S9, table S1, and Supplementary Discussion S3 describe flight repeatability experiments.

Beyond tolerating minor damage, our robot preserved its hovering flight accuracy after enduring critical damage. We introduced severe actuator damage by piercing a DEA with 10 needles and inducing an unclearable breakdown defect in another DEA. To restore flight, we performed laser-assisted repair for the DEA with an unclearable breakdown. Then, we commanded self-clearing for both DEAs and tuned the flight controller parameters. Figure S10 and movie S10 show two 12-s controlled hovering flights where the robot had two differently damaged DEAs. The maximum position, altitude, and attitude errors were comparable to those of the flights shown in Fig. 6.

Last, we removed 20% of the left-wing area from the robot module driven by the 10-pierced DEA. As shown in Fig. 1B, this robot had a 10-pierced DEA (Fig. 1C), a laser-recovered DEA (Fig. 1D), and a defective wing (Fig. 1E). Under these damages, the robot demonstrated a 12-s hovering flight (Fig. 7 and Movie 1) where the maximum deviation of altitude, lateral position, and body angles were 0.54 cm, 3.56 cm, and 3.1°, respectively (Fig. 7B). This flight quality was comparable to that of an undamaged robot (Fig. 7C). Figure S9 and Supplementary Discussion S3 show flight repeatability. These hovering flights highlighted the robot's damage resilience without compromising position and attitude accuracy—a key biomimetic capability absent in existing aerial robots.

DISCUSSION

In this work, we developed an aerial robot that can endure severe actuator and wing damage. Our flight demonstrations highlight that soft-actuated robots can simultaneously perform power-intensive tasks and exhibit animal-like resilience—a critical biomimetic capability that is absent in rigid-driven systems. Beyond demonstrating flight, the damage-resilient DEAs could be incorporated in other robots that need to function in hazardous natural environments alongside biological systems. Like animals, future robots will be able to nimbly traverse complex terrains and perform delicate tasks after experiencing unexpected damage.

This biomimetic capability is enabled by the proposed design, fabrication, and repair methods for soft artificial muscles. By optimizing electrode designs, we demonstrated power-dense (>700 W kg^{-1}) soft actuators that can survive more than 100 punctures and maintain flight-level performance. Compared with previous works (*23*, *26*) on self-clearing DEAs, our design process substantially improves DEA power density while maintaining resilience against piercing damage. We addressed a major limitation of self-clearing where unclearable defects can cause device failure. When an unclearable breakdown was introduced in a DEA, we demonstrated a laser-assisted repair method that can isolate the damaged site and recover performance. This repair method is broadly applicable to other DEAs, and it can substantially improve actuator size scalability and lifetime. Traditionally, the DEA performance and lifetime are limited by the defect that has the worst dielectric strength. In the fabrication process, the probability of introducing a severe defect grows linearly as DEA size increases. Our laser-assisted repair method can selectively isolate local defects and dissociate actuator size and the probability of having critical defects. This method can enable fabrication of substantially larger DEAs, benefiting broader applications of soft artificial muscles in other fields, such as haptics (*32*) and prosthetics (*33*).

More broadly, our laser ablation method can be extended into a method for patterning electrodes, which will benefit future designs of stretchable displays (*34*, *35*) and shape-morphing structures (*36*). In these devices, the electrodes have specifically designed patterns for achieving desired illuminated shapes or deformation. In the fabrication process, researchers use precut masks to pattern the electrodes, which has a coarse resolution of more than 200 μm (*20*). In this work, our laser spot size is less than 30 μm, which will lead to finer features and higher resolution compared with existing methods.

Despite demonstrating unique properties such as damage resilience, simultaneous actuation and sensing (*20*), and electroluminescence (*34*, *35*), DEAs lag behind rigid actuators in several key areas. DEAs require substantially higher driving voltages (500 V to 10 kV), and most of them have low transduction efficiencies (15 to 30%). These shortcomings pose major challenges for developing micro- and mesoscale (<20 g) power autonomous soft aerial robots. Toward achieving untethered flight (*37*) in soft driven robots, future work should focus on reducing DEA actuation voltages, improving transduction efficiencies, and developing compact power electronics and energy sources. In parallel, insect-scale soft aerial robots can be used to investigate collective insect behaviors such as assisted pollination or collective hive construction (*38*).

MATERIALS AND METHODS

Fabrication of robot components

The robot was designed and fabricated through existing methods (*20*, *35*, *39*, *40*). The robot weighed 680 mg and consisted of four modules. Each robot module weighed 155 mg and consisted of an airframe, two connecting bars, two transmissions, two wing hinges, two wings, and a DEA. Besides the DEA, all robot components were made on the basis of the smart composite manufacturing method. The airframe was made of 160-μm-thick carbon fiber laminates that were laser-cut and then hand-assembled. The connecting bars linked two ends of the DEAs and the robot transmission. They were made of fiberglass (FR-4) to isolate DEA voltages from the airframe. The robot transmission resembled a linear four-bar mechanism that had a transmission ratio of 2500 rad m^{-1}. It was made of 90-μm carbon fiber laminates and 25-μm polyimide (Kapton). The robot wing hinge connected the transmissions and the wings. It was made of a carbon fiber and a 12.7-μm Kapton flexure. The length and width of the flexures were 2.15 and 0.08 mm, respectively. The robot wing adopted a previous design (*39*), and the wingspan was 10 mm.

The DEA was also made of the same processes as described in a previous work (*39*). Here, all DEAs had seven elastomer (Elastosil P7670) layers and six alternating CNT electrode layers. The elastomer-electrode multilayer was 210 μm thick, and its length and width were 52 and 9 mm, respectively. Next, the multilayer was rolled into a cylindrical shell whose diameter and height were 4 and 9 mm, respectively. The CNT electrode was prepared using a vacuum filtration and stamping approach (*39*). To improve DEA resilience against piercing damage, we changed the CNT areal density compared with previous works. The CNT areal density relates to the amount of CNT solution (Nano-C Inc., Invisicon 3500) that was used when CNTs were transferred to a polytetrafluoroethylene filter (Sartorius 7022P). In Fig. 2E, the CNT areal density is reported in the unit of microliter per square centimeter, where we normalized the amount of CNT solution by filter area. To make electroluminescent DEAs, we embedded zinc sulfide (ZnS:Cu) particles in the elastomer layer (*35*). During actuation, the electric field excited the particles to emit light. This phenomenon was used to study electrode connectivity. If a region was lit, it implied that the local CNTs were connected. If a region became dark, it implied that the local CNTs were disconnected.

DEA blocked force, free displacement, and output power

To enable robotic flight, a DEA must have sufficient power density. We calculated a DEA's power density through quantifying its free displacement and blocked force as functions of the driving voltage (Fig. 1, F and G). In this work, the DEA's driving frequency was fixed to 400 Hz, because it corresponds to the robot's operating frequency. We placed a DEA under a Nano17 Titanium force sensor to measure its blocked force. To secure the DEA under the force sensor, we precompressed the DEA by about 0.05 N. Figure S2A shows the sensor measurement when an undamaged DEA was driven at 1500 V and 400 Hz. The red curve shows raw sensor data, and the blue curve shows the low-pass (1500-Hz cutoff frequency) filtered data. The DEA's blocked force was calculated as the zero-to-peak force. For this experiment, the blocked force was 0.24 N. The blocked force measurement method was adopted from a previous work (*20*).

We further measured the DEA's free displacement as a function of driving voltage. For each driving voltage, we recorded the DEA's motion using a high-speed camera at 22,000 frames per second. Figure S2B shows an image sequence of the DEA's motion at 1250 V and 400 Hz. We developed a custom computer vision method to track the DEA's top cap position in each frame. The DEA's free displacement was measured as its maximum elongation subtracted by its minimum contraction (fig. S2C). For this example (an undamaged DEA driven at 1250 V and 400 Hz), the DEA's free displacement was 0.73 mm. We used this method to measure the DEA's displacement at different operating voltages and frequencies. Figure S2D compares the free displacement of four DEAs. The damaged DEAs exhibited smaller free displacements at the same driving voltage.

On the basis of the blocked force and free displacement measurements, we calculated the DEA power density:

$$p = \frac{F_B \times \delta \times f}{2m} \tag{1}$$

where F_B is the blocked force, δ is the DEA displacement, f is the DEA operation frequency, and m is the DEA mass. In our experiments, the DEA was about 120 mg. This weight included the carbon fiber endcaps, glue, and the electrical connections. A DEA's output power in a robot strongly depends on the design of the mechanical system. In this work, we reported the DEA power density while it drove a flapping-wing robot.

DEA piercing damage

We designed conductive and insulating needles to perform piercing experiments. Figure S1A shows an insulating fiberglass needle and a conductive carbon fiber needle. The needles were designed as isolateral triangles where the base and height were 1 and 10 mm, respectively. Both types of needles were micromachined by an ultraviolet laser (LPKF ProtoLaser U4). The thicknesses of the fiberglass and the carbon fiber needles were 150 and 160 μm, respectively.

When a fiberglass needle pierced through a rolled DEA (fig. S1, B and C), it penetrated the elastomer-electrode multilayer 12 times. Figure S1C illustrates that the rolled DEA consisted of six layers, and the needle cut through these six layers twice, which was equivalent to making 12 punctures in the electrode-elastomer multilayer. When a DEA was pierced by 10 needles, it suffered 120 punctures in the electrode-elastomer multilayer.

The resistive sample tests (Fig. 2C) aimed to study the self-clearing of defects at the contact between a needle and the bulk CNT electrode. Figure S1E shows how R_{CNT}, R_{needle}, and R_{total} were measured. To calculate R_{contact}, we used the equation

$$R_{\mathrm{contact}} = R_{\mathrm{total}} - \frac{1}{2}R_{\mathrm{CNT}} - \frac{1}{2}R_{\mathrm{needle}} \tag{2}$$

Here, the factor of $\frac{1}{2}$ accounts for how R_{CNT} and R_{needle} were measured as shown in fig. S1E. We observed that R_{needle} and R_{CNT} remained unchanged before and after self-clearing, but R_{contact} changed from a finite value to infinity (Fig. 2D). This result shows that the self-clearing process disconnected local piercing damage from the bulk CNTs and did not affect the conductivity of bulk CNTs.

After the defects were cleared, the resistive sample became an open circuit. We continued to increase the voltage until observing device breakdown. This device breakdown was caused by a reduction of dielectric strength near the piercing location. This breakdown could be observed when there was a sudden increase in current in the sample. Figure S1F shows the current response of a test sample with a CNT areal density of 4.72 μl cm^{-2}. For each sample, we measured this breakdown voltage and reported it in Fig. 2E. Our amplifiers have a limit of 2 kV. If the test sample did not experience breakdown at 2 kV, then the breakdown voltage was marked as 2 kV. We reported the sample capacitances and resistances as functions of the number of piercing damages (Fig. 2H). The capacitance and resistance values were measured using a custom circuit from a previous work (*40*).

Furthermore, piercing damage had a dynamic influence on DEA free displacement. As shown in Fig. 1 (F to G), the 10-pierced DEA experienced 40 and 26% reduction of free displacement and blocked force, respectively. This difference was mainly caused by the mechanical constraint due to the fiberglass needles. During the free displacement experiment, these needles oscillated along with the DEA, dissipated energy, and reduced net motion. We designed an experiment in which we first measured the motion of a pierced DEA and then removed the needle and remeasured the motion. Taking out the needle did not recover previously self-cleared CNTs; hence, it represented removing the needle's mechanical influence. Figure S2 (E to G) quantifies this influence by comparing the DEA's free displacement before and after a needle was removed. In fig. S2E, a DEA was pierced by a needle, and then we measured its peak-to-peak motion at the operating condition of 1200 V and 500 Hz. Next, we removed the needle and made the measurement again at the same operating condition (fig. S2F). The tracked instantaneous DEA motions are compared in fig. S2G. After the needle was removed, the peak-to-peak motion increased from 0.65 to 0.70 mm. This mechanical influence was negligible in blocked force experiments, because the DEA motion was constrained by the force sensor.

Two-step laser ablation and self-clearing method for isolating unclearable damage

We developed a two-step process for isolating unclearable breakdowns. In contrast to piercing damage that could be recovered through self-clearing, there was severe damage that self-clearing alone could not isolate. Through experiments, we found that removing materials (drilling a large hole), making punctures with a large diameter needle, and inducing burning damage could cause unclearable defects. In this work, we introduced unclearable defects (Figs. 1D and 3G) by piercing a DEA with a 16-gauge needle (with a diameter of 1.65 mm). Then, we performed self-clearing and observed severe burning and device failure (Fig. 3, G to I).

To isolate these unclearable defects, we used a custom DPSS laser (fig. S4A). We placed a damaged DEA under the microscope, focused on the DEA's top surface, and then commanded the laser to trace a path that encircled the defect. The laser beam penetrated the elastomer-electrode multilayer, and most of the laser power was absorbed by the CNTs. The thermal energy from the laser beam degraded local CNTs and caused an increase in local resistance. Next, we performed self-clearing where most of the voltage was applied across the laser-ablated CNTs. The thermal energy concentrated near the laser-ablated region, and it disconnected the defect from the bulk CNTs. Our laser-assisted defect isolation method was different from existing laser ablation methods (*41*, *42*) used in DEA fabrications. Traditionally, CO_2 lasers are used to pattern the electrode. These approaches remove CNTs on the top layer, and they do not penetrate elastomers in multilayer DEAs. CO_2 lasers have larger spot sizes (>100 μm), so they cannot degrade local CNTs without damaging elastomers and the bulk CNTs. These existing approaches are applied in DEA fabrication processes, but they cannot be used in DEA repair.

In this two-step defect isolation method, it was critical to choose an appropriate laser setting. We measured the laser power and pulse energy as a function of the repetition rate (fig. S4B). Using different repetition rates (20 to 240 kHz), we made a series of cuts on a DEA sample (fig. S4C). At 20 kHz (fig. S4D), the laser power was too high, and it severely damaged the elastomer. This exposed the CNTs and could not recover a DEA. At 80 kHz (fig. S4E), we observed that the laser beam width was around 20 to 30 μm. In a resistive test, the sample resistance increased by about 100%. This was a satisfactory cut where the second self-clearing step could isolate the defect. At 240 kHz (fig. S4F), the laser power was too low, and we could not measure any change in DEA resistance. This was insufficient for concentrating the thermal energy in the second self-clearing step. In this work, the laser pulse frequency and beam speed were set to 80 kHz and 200 mm s^{-1}, respectively. At this setting, the laser beam could reliably isolate defects in DEAs that consisted of six electrodes and seven elastomer layers. The elastomer-electrode multilayer thickness was in the range of 200 to 220 μm. We focused the laser beam on the top surface of the elastomer-electrode multilayer. The laser beam was tapered as it penetrated the DEA (fig. S4G). The top and bottom view images (fig. S4G) show that the laser path widths were 26 and 19 μm, respectively. In the experiments, this tapered cut did not have noticeable electrical or mechanical influence on DEA performance. The details of the laser settings and electrical modeling are described in Supplementary Discussion S2.

For a robot driven by an undamaged DEA, the robot takeoff voltage was 1450 V, corresponding to a blocked force of 0.22 N. The robot's wing stroke amplitude was about 45°, corresponding to a DEA displacement of 0.63 mm. At the 400-Hz flapping frequency, the DEA's power density was 231 W kg^{-1}. At the DEA's maximum operating voltage of 1800 V, the DEA's blocked force and in-robot displacement increased to 0.36 N and 1.2 mm, respectively, and consequently, the DEA's power density increased to 725 W kg^{-1}. On the basis of the blocked force and robot static flapping experiments, we further calculated the power density of the 1-pierced, 10-pierced, and the laser-recovered DEAs. The maximum power densities of these DEAs were 592, 401, and 542 W kg^{-1}, respectively. All of these damaged DEAs exhibited sufficient power density (>200 W kg^{-1}) for demonstrating controlled flight.

DEA dc and ac tests and measurements of equivalent resistance and capacitance

We conducted two types of self-clearing experiments: dc and ac tests. In dc experiments such as the ones shown in Figs. 2G and 3I, we commanded step input voltages. The DEA behaved as a series resistor-capacitor circuit. When the voltage was constant, the DEA current was 0 mA. When the voltage increased discontinuously at a step, the current response resembled an impulse function. In dc clearing, a defect or a local dielectric breakdown could cause a leakage current (Fig. 2G). Once the defect was disconnected from the bulk electrode, the leakage current was reduced to 0 mA.

We also conducted ac self-clearing experiments where we used electroluminescence to visualize CNT connectivity (Figs. 2I and 3C). In ac clearing experiments, we commanded a sinusoidal driving signal. We used a high driving frequency of 3000 Hz in Fig. 3C, because the emitted light intensity was proportional to the driving frequency. Both dc and ac clearing could disconnect defects from the bulk electrode. The ac tests were also used to measure the equivalent DEA capacitance and resistance (Fig. 2H). We assembled a custom circuit based on our previous work (*39*). The DEA resistance and capacitance were used to estimate the DEA's bandwidth, and this method is discussed in Supplementary Discussion S1.

Supplementary Materials

This PDF file includes:
Supplementary Discussion S1 to S3
Figs. S1 to S10
Table S1

Other Supplementary Material for this manuscript includes the following:
Movies S1 to S10

REFERENCES AND NOTES

1. Y. Li, H. Sato, B. Li, Feedback altitude control of a flying insect-computer hybrid robot. *IEEE Trans. Robot.* **37**, 2041–2051 (2021).
2. F. T. Muijres, N. A. Iwasaki, M. J. Elzinga, J. M. Melis, M. H. Dickinson, Flies compensate for unilateral wing damage through modular adjustments of wing and body kinematics. *Interface Focus* **7**, 20160103 (2017).
3. G. J. Vermeij, Unsuccessful predation and evolution. *Am. Nat.* **120**, 701–720 (1982).
4. J.-H. Dirks, D. Taylor, Veins improve fracture toughness of insect wings. *PLOS ONE* **7**, e43411 (2012).
5. H. V. Phan, H. C. Park, Mechanisms of collision recovery in flying beetles and flapping-wing robots. *Science* **370**, 1214–1219 (2020).
6. P. Sareh, P. Chermprayong, M. Emmanuelli, H. Nadeem, M. Kovac, Rotorigami: A rotary origami protective system for robotic rotorcraft. *Sci. Robot.* **3**, eaah5228 (2018).
7. S. Sun, G. Cioffi, C. D. Visser, D. Scaramuzza, Autonomous quadrotor flight despite rotor failure with onboard vision sensors: Frames vs. events. *IEEE Robot. Autom. Lett.* **6**, 580–587 (2021).
8. Z. Tu, F. Fei, L. Liu, Y. Zhou, X. Deng, Flying with damaged wings: The effect on flight capacity and bio-inspired coping strategies of a flapping wing robot. *IEEE Robot. Autom. Lett.* **6**, 2114–2121 (2021).
9. M. Karásek, F. T. Muijres, C. De Wagter, B. D. Remes, G. C. de Croon, A tailless aerial robotic flapper reveals that flies use torque coupling in rapid banked turns. *Science* **361**, 1089–1094 (2018).

10. K. Y. Ma, P. Chirarattananon, S. B. Fuller, R. J. Wood, Controlled flight of a biologically inspired, insect-scale robot. *Science* **340**, 603–607 (2013).
11. E. Acome, S. K. Mitchell, T. G. Morrissey, M. B. Emmett, C. Benjamin, M. King, M. Radakovitzand, C. Keplinger, Hydraulically amplified self-healing electrostatic actuators with muscle-like performance. *Science* **359**, 61–65 (2018).
12. C. D. Onal, X. Chen, G. M. Whitesides, D. Rus, in *Robotics Research* (Springer, New York, 2017), pp. 525–540.
13. E. J. Markvicka, M. D. Bartlett, X. Huang, C. Majidi, An autonomously electrically self-healing liquid metal–elastomer composite for robust soft-matter robotics and electronics. *Nat. Mater.* **17**, 618–624 (2018).
14. R. A. Bilodeau, R. K. Kramer, Self-healing and damage resilience for soft robotics: A review. *Front. Robot. AI* **4**, 48 (2017).
15. M. D. Bartlett, M. D. Dickey, C. Majidi, Self-healing materials for soft-matter machines and electronics. *NPG Asia Mater.* **11**, 1–4 (2019).
16. C.-H. Li, C. Wang, C. Keplinger, J.-L. Zuo, L. Jin, Y. Sun, P. Zheng, Y. Cao, F. Lissel, C. Linder, X.-Z. You, Z. Bao, A highly stretchable autonomous self-healing elastomer. *Nat. Chem.* **8**, 618–624 (2016).
17. S. Terryn, J. Brancart, D. Lefeber, G. V. Assche, B. Vanderborght, Self-healing soft pneumatic robots. *Sci. Robot.* **2**, eaan4268 (2017).
18. N. Kellaris, V. G. Venkata, G. M. Smith, S. K. Mitchell, C. Keplinger, Peano-HASEL actuators: Muscle-mimetic, electrohydraulic transducers that linearly contract on activation. *Sci. Robot.* **3**, eaar3276 (2018).
19. Y. Shi, E. Askounis, R. Plamthottam, T. Libby, Z. Peng, K. Youssef, J. Pu, R. Pelrine, Q. Pei, A processable, high-performance dielectric elastomer and multilayering process. *Science* **377**, 228–232 (2022).
20. Y. Chen, H. Zhao, J. Mao, P. Chirarattananon, E. F. Helbling, N. P. Hyun, D. R. Clarke, R. J. Wood, Controlled flight of a microrobot powered by soft artificial muscles. *Nature* **575**, 324–329 (2019).
21. G. Li, X. Chen, F. Zhou, Y. Liang, Y. Xiao, X. Cao, Z. Zhang, M. Zhang, B. Wu, S. Yin, Y. Xu, H. Fan, Z. Chen, W. Song, W. Yang, B. Pan, J. Hou, W. Zou, S. He, X. Yang, G. Mao, Z. Jia, H. Zhou, T. Li, S. Qu, Z. Xu, Z. Huang, Y. Luo, T. Xie, J. Gu, S. Zhu, W. Yang, Self-powered soft robot in the Mariana Trench. *Nature* **591**, 66–71 (2021).
22. X. Ji, X. Liu, V. Cacucciolo, M. Imboden, Y. Civet, A. E. Haitami, S. Cantin, Y. Perriard, H. Shea, An autonomous untethered fast soft robotic insect driven by low-voltage dielectric elastomer actuators. *Sci. Robot.* **4**, eaaz645 (2019).
23. W. Yuan, L. Hu, Z. Yu, T. Lam, J. Biggs, S. M. Ha, D. Xi, B. Chen, M. K. Senesky, G. Grüner, Q. Pei, Fault-tolerant dielectric elastomer actuators using single-walled carbon nanotube electrodes. *Adv. Mater.* **20**, 621–625 (2008).
24. Y. Zhang, C. Ellingford, R. Zhang, J. Roscow, M. Hopkins, P. Keogh, T. McNally, C. Bowen, C. Wan, Electrical and mechanical self-healing in high-performance dielectric elastomer actuator materials. *Adv. Funct. Mater.* **29**, 1808431 (2019).
25. Z. Peng, Y. Shi, N. Chen, Y. Li, Q. Pei, Stable and high-strain dielectric elastomer actuators based on a carbon nanotube-polymer bilayer electrode. *Adv. Funct. Mater.* **31**, 2008321 (2021).
26. S. Jiang, C. Tang, X.-J. Liu, H. Zhao, Long-life-cycle and damage-recovery artificial muscles via controllable and observable self-clearing process. *Adv. Eng. Mater.* **24**, 2101017 (2022).
27. L. Duan, J.-C. Lai, C.-H. Li, J.-L. Zuo, A dielectric elastomer actuator that can self-heal integrally. *ACS Appl. Mater. Interfaces* **12**, 44137–44146 (2020).
28. J. Xu, Y. Dong, Z. Jiang, L. Tang, X. Chen, Z. Yao, K. Cao, Self-healing high-performance dielectric elastomer actuator with novel liquid-solid interpenetrating structure. *Compos. A: Appl. Sci. Manuf.* **149**, 106519 (2021).
29. K. Chakraborty, K. VijayRaghavan, R. Gunage, A method to injure, dissect and image indirect flight muscle of Drosophila. *Bio Protoc.* **8**, e2860 (2018).
30. R. Dukas, L. Dukas, Coping with nonrepairable body damage: Effects of wing damage on foraging performance in bees. *Anim. Behav.* **81**, 635–638 (2011).
31. R. J. Wood, E. Steltz, R. S. Fearing, Nonlinear performance limits for high energy density piezoelectric bending actuators, in *Proceedings of the 2005 IEEE International Conference on Robotics and Automation* (IEEE, 2005), pp. 3633–3640.
32. X. Ji, X. Liu, V. Cacucciolo, Y. Civet, A. E. Haitami, S. Cantin, Y. Perriard, H. Shea, Untethered feel-through haptics using 18-μm thick dielectric elastomer actuators. *Adv. Funct. Mater.* **31**, 2006639 (2021).
33. A. Bruschi, D. M. Donati, P. Choong, E. Lucarelli, G. Wallace, Dielectric elastomer actuators, neuromuscular interfaces, and foreign body response in artificial neuromuscular prostheses: A review of the literature for an in vivo application. *Adv. Healthc. Mater.* **10**, e2100041 (2021).
34. J. Wang, C. Yan, K. J. Chee, P. S. Lee, Highly stretchable and self-deformable alternating current electroluminescent devices. *Adv. Mater.* **27**, 2876–2882 (2015).
35. S. Kim, Y.-H. Hsiao, Y. Chen, J. Mao, Y. Chen, FireFly: An insect-scale aerial robot powered by electroluminescent soft artificial muscles. *IEEE Robot. Autom. Lett.* **7**, 6950–6957 (2022).
36. E. Hajiesmaili, N. M. Larson, J. A. Lewis, D. R. Clarke, Programmed shape-morphing into complex target shapes using architected dielectric elastomer actuators. *Sci. Adv.* **8**, eabn9198 (2022).
37. D. Floreano, R. J. Wood, Science, technology and the future of small autonomous drones. *Nature* **521**, 460–466 (2015).
38. K. Zhang, P. Chermprayong, F. Xiao, D. Tzoumanikas, B. Dams, S. Kay, B. B. Kocer, A. Burns, L. Orr, C. Choi, D. D. Darekar, W. Li, S. Hirschmann, V. Soana, S. A. Ngah, S. Sareh, A. Choubey, L. Margheri, V. M. Pawar, R. J. Ball, C. Williams, P. Shepherd, S. Leutenegger, R. Stuart-Smith, M. Kovac, Aerial additive manufacturing with multiple autonomous robots. *Nature* **609**, 709–717 (2022).
39. Z. Ren, S. Kim, X. Ji, W. Zhu, F. Niroui, J. Kong, Y. Chen, A high-lift micro-aerial-robot powered by low-voltage and long-endurance dielectric elastomer actuators. *Adv. Mater.* **34**, 2106757 (2022).
40. Y. Chen, S. Xu, Z. Ren, P. Chirarattananon, Collision resilient insect-scale soft-actuated aerial robots with high agility. *IEEE Trans. Robot.* **37**, 1752–1764 (2021).
41. J. Shintake, Y. Piskarev, S. H. Jeong, D. Floreano, Ultrastretchable strain sensors using carbon black-filled elastomer composites and comparison of capacitive versus resistive sensors. *Adv. Mater. Technologies* **3**, 1700284 (2018).
42. O. A. Araromi, S. Rosset, H. R. Shea, High-resolution, large-area fabrication of compliant electrodes via laser ablation for robust, stretchable dielectric elastomer actuators and sensors. *ACS Appl. Mater. Interfaces* **7**, 18046–18053 (2015).

Acknowledgments: Y.C. is grateful to Y. Zhu for discussion and proofreading. We thank the reviewers and the editor for feedback on this manuscript. **Funding:** This work is supported by the National Science Foundation grant 2202477 (Y.C.) and a MathWorks Fellowship (S.K. and Z.R.) **Author contributions:** S.K., Y.-H.H., and Y.C. initiated the project, designed the experiments, and fabricated the robots. S.K., Y.-H.H., Y.L., Z.R., and Y.C. conducted the experiments. W.Z. and F.N. took the scanning electron microscope images. All authors analyzed the data. Y.C. wrote the paper. All authors discussed the results and commented on the manuscript. Conceptualization: Y.C. Methodology: S.K., Y.-H.H., and Y.C. Software: Y.-H.H., Z.R., and Y.C. Validation: S.K., Y.-H.H., and Y.C. Formal analysis: S.K., Y.-H.H., Y.L., W.Z., Z.R., F.N., and Y.C. Investigation: S.K., Y.-H.H., and Y.C. Resources: F.N. and Y.C. Data curation: S.K., Y.-H.H., and Y.C. Writing (original draft): S.K., Y.-H.H., and Y.C. Writing (review and editing): S.K., Y.-H.H., Y.L., W.Z., F.N., and Y.C. Visualization: S.K., Y.-H.H., W.Z., F.N., and Y.C. Supervision: Y.C. Project administration: Y.C. Funding acquisition: Y.C. **Competing interests:** The authors declare that they have no competing interests. **Data and materials availability:** All data needed to support the conclusions of this manuscript are included in the main text or Supplementary Materials.

Submitted 20 October 2022
Accepted 20 February 2023
Published 15 March 2023
10.1126/scirobotics.adf4278

Science Robotics

Laser-assisted failure recovery for dielectric elastomer actuators in aerial robots

Suhan Kim, Yi-Hsuan Hsiao, Younghoon Lee, Weikun Zhu, Zhijian Ren, Farnaz Niroui, and Yufeng Chen

Sci. Robot. **8** (76), eadf4278. DOI: 10.1126/scirobotics.adf4278

Science Robotics (ISSN 2470-9476) is published by the American Association for the Advancement of Science. 1200 New York Avenue NW, Washington, DC 20005. The title *Science Robotics* is a registered trademark of AAAS.